CHEMISTRY OF MATERIALS

pubs.acs.org/cm

Article

Insights into Nd^{III} to Yb^{III} Energy Transfer and Its Implications in Luminescence Thermometry

Mariangela Oggianu,[▽] Valentina Mameli,[▽] Miguel A. Hernández-Rodríguez,[▽] Noemi Monni, Manuel Souto, Carlos D.S. Brites, Carla Cannas, Fabio Manna, Francesco Quochi, Enzo Cadoni, Norberto Masciocchi, Albano N. Carneiro Neto,* Luís D. Carlos,* and Maria Laura Mercuri*

Cite This: *Chem. Mater.* 2024, 36, 3452−3463

Read Online

ACCESS | Metrics & More | Article Recommendations | Supporting Information

ABSTRACT: This work challenges the conventional approach of using Nd^{III} $^4F_{3/2}$ lifetime changes for evaluating the experimental Nd^{III} → Yb^{III} energy transfer rate and efficiency. Using near-infrared (NIR) emitting Nd:Yb mixed-metal coordination polymers (CPs), synthesized via solvent-free thermal grinding, we demonstrate that the Nd^{III} [$^2H_{11/2}$ → $^4I_{15/2}$] → Yb^{III} [$^2F_{7/2}$ → $^2F_{5/2}$] pathway, previously overlooked, dominates energy transfer due to superior energy resonance and *J*-level selection rule compatibility. This finding upends the conventional focus on the Nd^{III} [$^4F_{3/2}$ → $^4I_{11/2}$] → Yb^{III} [$^2F_{7/2}$ → $^2F_{5/2}$] transition pathway. We characterized $Nd_{0.890}Yb_{0.110}(BTC)$-$(H_2O)_6$ as a promising cryogenic NIR thermometry system and employed our novel energy transfer understanding to perform simulations, yielding theoretical thermometric parameters and sensitivities for diverse Nd:Yb ratios. Strikingly, experimental thermometric data closely matched the theoretical predictions, validating our revised model. This novel perspective on Nd^{III} → Yb^{III} energy transfer holds general applicability for the Nd^{III}/Yb^{III} pair, unveiling an important spectroscopic feature with broad implications for energy transfer-driven materials design.

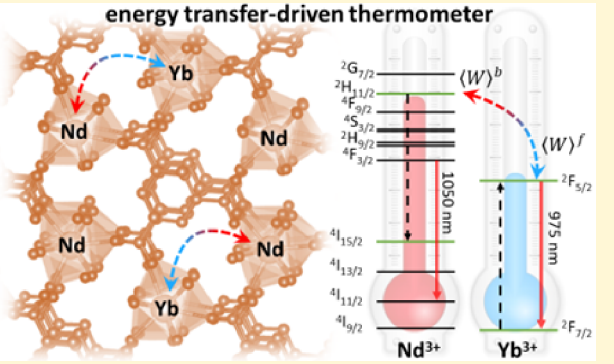

INTRODUCTION

Temperature is a critical physical parameter and its accurate detection is of paramount importance in many research fields ranging from climate, metrology, aerospace, nanomedicine, production plants, and food storage.[1,2] During the past decade, novel temperature sensors have emerged that have the potential to substitute resistance thermometry.[3] All examples are based on temperature-induced changes in the material's chemical and physical properties, such as volume, electrical conductivity, or photoluminescence.

Among these is luminescence thermometry, which was developed as a remote temperature sensing technique that relies on the temperature dependency of luminescence features (e.g., band shape, peak energy or intensity, and excited state lifetimes and risetimes) of a phosphor to measure temperature.[4−8] This technique provides precise thermal readouts with superior spatial resolution in short acquisition times. Noticeably, luminescent thermometers can operate in distinct temperature regions, from cryogenic temperatures (<100 K), of interest in cryobiology, aerospace, nuclear fusion, and the development of superconducting magnets,[9−13] to high temperatures (>400 K) with potential applications in heavy industry,[14] covering also the so-called physiological temperature range (298−323 K), of interest in biomedicine.[15]

Up to now, a plethora of luminescent materials, such as quantum dots, organic dyes, lanthanide-doped nanoparticles, and lanthanide complexes have been largely investigated for luminescence thermometry.[5] Among them, trivalent lanthanide (Ln^{III}) ions, including chelate complexes,[16,17] polymers,[18,19] metal−organic frameworks (MOFs),[20,21] and organic−inorganic hybrids molecular probes,[22,23] are promising materials for thermal sensing, given their typical long lifetimes (10^{-3} s range), characteristic sharp emission, and high emission quantum yields, emitting in the ultraviolet, visible, and near-infrared spectral regions.[17,24,25]

It is well-known that Ln^{III} centers cannot efficiently absorb light due to forbidden 4f−4f transitions.[26] To overcome this, a challenging strategy for the fabrication of highly performant Ln-based materials, including luminescent thermometers, lies in the incorporation of luminescent linkers as a suitable *antenna*, thereby being able to absorb and transfer energy to the Ln^{III} centers.[27] Lanthanide-based coordination polymers

Received: February 8, 2024
Revised: March 12, 2024
Accepted: March 13, 2024
Published: March 28, 2024

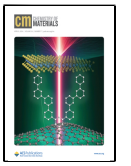

(CPs) and MOFs are excellent candidates for optical sensors due to their ability to show both ligand-centered and metal-centered luminescence. The proper choice of the luminescent building blocks, both Ln^{III} ions (metallic nodes) and functional organic linkers, is crucial to designing new CPs for thermal sensing applications showing different pathways of energy exchange, including intensity-based and ratiometric thermometers.[28]

Recently, mixed Ln'Ln"-MOFs thermometers have been developed where the intensity ratio of two emissions from different lanthanide ions, commonly Tb^{III} and Eu^{III}, is used as the thermometric parameter,[20,21,29,30] based on emissions in the visible spectral range. Cui et al. reported on the first example of a luminescent thermometer, based on mixed-Eu^{III}/Tb^{III} MOF and $Eu_{0.0069}Tb_{0.9931}$-DMBDC (DMBDC = 2,5-dimethoxy-1,4-benzene-dicarboxylate), showing a significant temperature-dependent photoluminescence in the 10−300 K range.[20] Besides the Eu^{III}/Tb^{III} pair, the Nd^{III} and Yb^{III} ions have been receiving growing interest given their harmless emission wavelength and deep penetration length in biological tissues.[31−38] However, all of the works reported so far rely on an unpredictable serendipitous approach, lacking a comprehensive elucidation of the thermometric performance rooted in donor-to-acceptor energy transfer mechanisms between Ln^{III} ions. This absence of understanding hinders the rational optimization of these materials.

Therefore, in this study, we employ a novel class of NIR-emitting Yb/Nd CPs based on the 1,3,5-benzentricarboxylic acid (H_3BTC) organic linker to deeply investigate the Nd−Yb energy transfer process and quantitatively illustrate its influence on the thermometric properties of the materials. Then, the objective of the manuscript is to fully understand the underlying energy transfer mechanisms, and their crucial implications for optimizing energy transfer-driven ratiometric luminescent thermometers, rather than looking for a higher thermometric performance. Two different classes have been synthesized through a solvent-free thermal grinding method, formulated as $Nd_xYb_{(1-x)}(BTC)(H_2O)_6$ (x = 1 (**1**); x = 0.943 (**2**); x = 0.953 (**3**); x = 0.890 (**4**)) and $Nd_xYb_{(1-x)}(BTC)$ (x = 0.017 (**5**), x = 0 (**6**)). Single lanthanide Nd-CPs and Yb-CPs have also been prepared as reference samples. The obtained materials have been morphologically, structurally, and thermally characterized and their photophysical processes (10−300 K) have been studied to determine the temperature dependence of the Nd^{III}-to-Yb^{III} energy transfer processes in a representative sample, $Nd_{0.890}Yb_{0.110}(BTC)(H_2O)_6$ (**4**) using the Nd-BTC (**1**) as a reference.

We demonstrate, both from experimental measurements and theoretical calculations, that the experimental Ln-to-Ln energy transfer rate (W_{exp})[39]

$$W_{exp} = \frac{1}{\tau_{DA}} - \frac{1}{\tau_{D}} \quad (1)$$

and the energy transfer efficiency (η_{ET})[40,41]

$$\eta_{ET} = 1 - \frac{\tau_{DA}}{\tau_{D}} \quad (2)$$

(τ_D and τ_{DA} are the lifetimes of the emitting level of the donor in the absence and presence of acceptors, respectively) are not valid for the specific case of Nd^{III}−Yb^{III} energy transfer when Nd^{III} $^4F_{3/2} \rightarrow {}^4I_{11/2}$ emission lifetimes are monitored for $Nd(BTC)(H_2O)_6$ (τ_D) and $Nd_xYb_{(1-x)}(BTC)(H_2O)_6$ (τ_{DA}) CPs. We can anticipate that the reason behind this is that the $^4F_{3/2} \rightarrow {}^4I_{11/2}$ is not an effective pathway in the Nd^{III}−Yb^{III} energy transfer process as other Nd^{III} transitions (e.g., $^2H_{11/2} \rightarrow {}^4I_{15/2}$) are responsible for the energy transfer process. Thus, a new point of view regarding the Nd^{III}−Yb^{III} energy transfer for excitation energies not being resonant with the $^4F_{3/2}$ energy level is herein pointed out, contrary to what is reported in the literature.[40,42−47]

Experimental Section. *Synthesis.* NIR emitter-based Ln′Ln″-CPs-CPs were synthesized through a solvent-free grinding method. $Ln(NO_3)_3{\cdot}6(H_2O)$ (Ln^{III} = Yb, Nd) and 1,3,5-benzenetricarboxylic acid (H_3BTC, trimesic acid) were mixed in a 1:1 ratio and ground for 5 min, and then thermally treated at 120 °C for 24 h, exploiting both mechanical and thermal energies (Scheme 1). This method, as reported by Liu et al.,[48] offers a valid alternative for rapid, eco-friendly, and large-scale preparation of luminescent Ln-CPs/MOFs, avoiding the production of a large amount of solvent waste.

Scheme 1. Schematic Representation of the Thermal Grinding Process

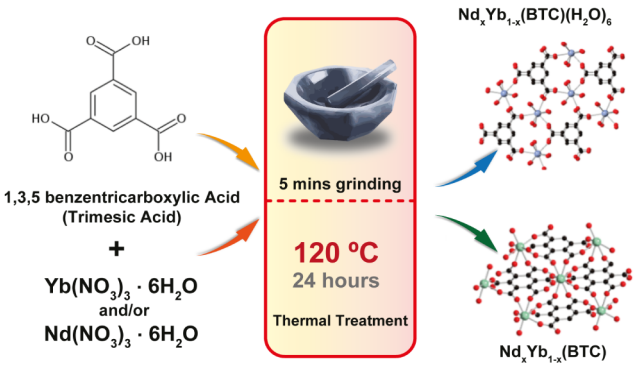

By adding to the precursor mixture a second Ln^{III} ion, with molar ratio in the 5 to 20%, compounds formulated as $Nd_xYb_{(1-x)}(BTC)(H_2O)_6$ (x = 1 (**1**); x = 0.943 (**2**); x = 0.953 (**3**); x = 0.890 (**4**)) and $Nd_xYb_{(1-x)}BTC$ (x = 0.017 (**5**), x = 0 (**6**)) are obtained in the form of microcrystalline powder.

The materials have been fully characterized by powder X-ray diffraction (PXRD) and Fourier transform infrared spectroscopy (FT-IR), induced coupled plasma mass spectrometry (ICP-MS), scanning electron microscopy−energy dispersive X-ray (SEM-EDX) and thermal gravimetric analysis (TGA).

The synthetic process was monitored by PXRD, as shown in Figure S1 for the formation of Yb(BTC). When the precursors of **6** [H_3BTC acid and $Yb(NO_3)_3{\cdot}6(H_2O)$] are mixed and milled for 30 s in an agate mortar, no formation of new compounds was detected. However, just after 1 min of milling, most of the precursor's diffraction peaks disappeared, and a few barely visible peaks, attributed to residual trimesic acid, remained. For longer milling times (3 to 5 min), a sort of amorphization process occurred, confirming the hypothesis originally provided by Liu et al.;[48] diffraction peaks progressively disappear, and the background level increases and becomes nonmonotonic. At this stage, the milled powders turned into a slurry. Treating this slurry at 120 °C led, after water elimination, to the formation of the desired Yb(BTC) CP. To verify if the grinding step had a direct role in the formation of Yb(BTC), the pristine mixture was also thermally treated, skipping the milling step. The PXRD analysis (see Figure S1) showed the obtainment of unknown crystal phases

https://doi.org/10.1021/acs.chemmater.4c00362
Chem. Mater. 2024, 36, 3452−3463

together with some residual reactants. Thus, the residual water present in the slurry could favor the reaction, as liquid-assisted grinding is used to facilitate mechanochemical reactions in disparate fields.[49−51] Finally, the addition of a washing step by water and then ethanol allowed for purification of the product in the case of residues of the precursor mixture.

Crystal Structures. Compounds **1**−**6** are obtained as microcrystalline powders only. Hence, to determine their crystal structure, we resorted to PXRD (performed on **1** and **6** samples only), due to the isomorphous character of species **1** to **4** and, separately, **5** and **6**. Compound **1** crystallizes in the monoclinic space group *Cc*, as a neutral polymeric framework, isostructural with a previously reported Gd^{III}-based species.[52] The asymmetric unit of **1**, shown in Figure 1A, consists of one Nd^{III} ion, one fully deprotonated BTC unit, and six water molecules, all bound to the rare earth cation. Each metal ion is *ennea*-coordinated, surrounded by nine oxygen atoms, three from (three different) BTC linkers and six from water molecules, leading to the $Nd(BTC)(H_2O)_6$ formulation. The Nd^{III} ions, linked through BTC ligands, form parallel 1D ribbons running along the $\vec{b}$ axis, as reported in Figure 1B. The stacking of these ribbons interconnected through a bevy of hydrogen bonds involving the H atoms of the coordinating water molecules, leads to a dense 3D framework (Figure 1C).

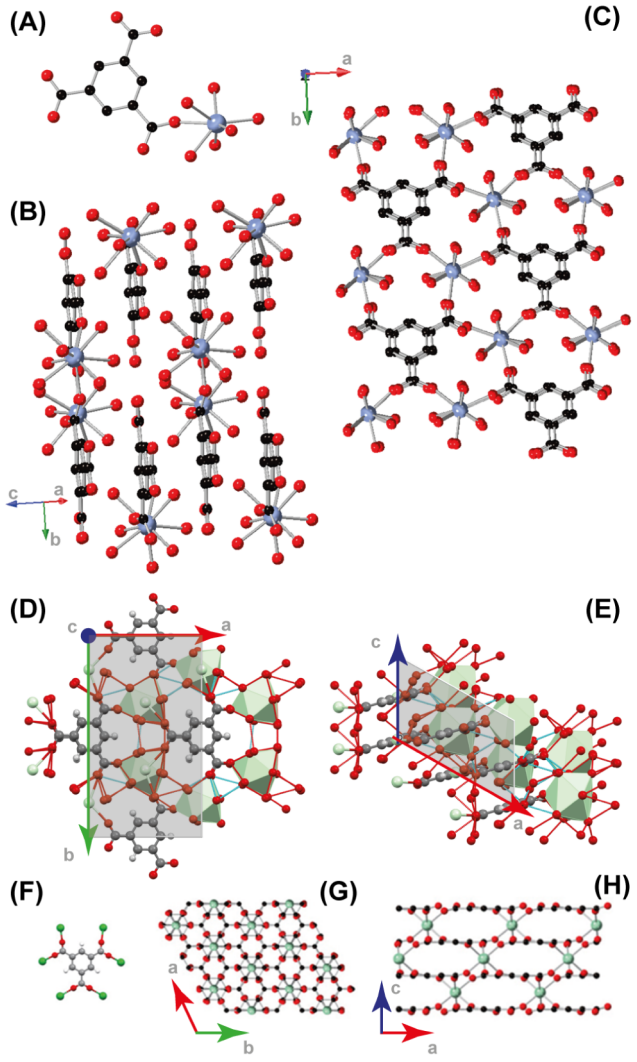

Figure 1. View of (A) the asymmetric unit of **1**, (B) 1D ribbons running parallel to the *b*-axis, and (C) stacked ribbons in the *ab* plane [001 view]. Sketch of the rich 3D hydrogen-bond framework (dashed red contacts) viewed along the (D) *c*- and (E) *b*-axis. View of (F) one BTC linker coordinating six Yb^{III} ions, (G) 3D CP in the *ab* plane, showing Yb^{III} ions stacked along the same *c* axis of aromatic BTC ring, (H) 3D CP in the *ac* plane, evidencing Yb^{III} and BTC lying in different planes. The black, red, and pastel (green) spheres represent the C, O, and Nd (Yb) atoms, respectively, while H atoms are omitted for clarity.

Figure 1D,E depicts the *ennea*-coordinated Nd atoms as green polyhedra and dashed red contacts indicate the rich 3D framework of hydrogen bonding, interlinking the different coordination spheres: the Nd−O bond distances are reported in Table S1. Note that, as restraints were introduced in the final Rietveld refinement cycles to stabilize the otherwise untreatable refinement diverging to an unphysical model, the obtained values mostly mirrored the numerical limits imposed of the Nd−O distances rather than their true similarity, or their dispersion.

Thermogravimetric analysis showed that all six coordinated water molecules can be completely removed by heating **1**, the hexahydrate $Nd(BTC)(H_2O)_6$ phase, at 130 °C (*vide infra*), leading to an amorphous material. The anhydrous Yb(BTC) (**6**) crystallizes as a complex 3D framework in the trigonal $R\bar{3}c$ space group. Its asymmetric unit consists of (a fraction of) one Yb^{III} ion and 1/6 of the fully deprotonated BTC ligand (both lying on special positions of -3 point symmetry). The coordination sphere of each metal ion is composed of six oxygen atoms belonging to six distinct BTC linkers with a Yb−O bond distance of 2.259(3) Å, which, in turn, coordinate six Yb^{III} ions in the μ_6 bridging coordination mode (Figure 1F).

This generates a 3D CP, where BTC aromatic rings, orderly stacked along the *c*-axis (Figure 1G), show intercalated Yb^{III} ions located midway at a distance of 1.56 Å (*c*/12) from the virtual plane containing the neighboring (and coordinating) BTC moieties. Indeed, when **6** is observed in the *ac* plane, as shown in Figure 1H, it is evident how all the Yb^{III} ions lie on a different, but parallel, plane than BTC linkers, forming a dense structure with no accessible cavities, with nonbonding $Yb^{III}\cdots Yb^{III}$ distances of 6.00 (out of plane) and 8.88 Å (in plane), heavily minimizing Coulombic repulsion.

In line with the structural model presented here, thermogravimetric analysis confirmed the anhydrous character of **6** (*vide infra*). The PXRD analysis (Figure 2) confirmed the obtainment of two different structures (*vide supra*), depending on the x content: the Nd-rich samples (**2**−**4**) feature the structure of the hydrated $Nd(BTC)(H_2O)_6$−CP (**1**), whereas the Yb-rich samples **5** and **6** are anhydrous and isostructural. Other intermediate substitution ratios (Nd:Yb 50:50 and 30:70) were also tested (Figure S2), but PXRD revealed the formation of polyphasic mixtures where hydrated and anhydrous phases coexist. Thus, it appears that Nd^{III} and Yb^{III} act as structure-directing agents for the hydrated and anhydrous phases, respectively, if they dominate in the precursor's mixture.

The results from our complete PXRD analysis also include an estimate of the specific surface areas (SSA) of our materials. As derived by the numerical analysis described in Text S1, SSA values fall well below 100 $m^2 \cdot g^{-1}$ (in line with the experimental BET values reported in the Experimental section). Note that porous materials possess much larger SSA values (in $m^2 \cdot g^{-1}$, 300−5000 for activated carbons, 1000 for zeolites, and up to

https://doi.org/10.1021/acs.chemmater.4c00362
Chem. Mater. 2024, 36, 3452−3463

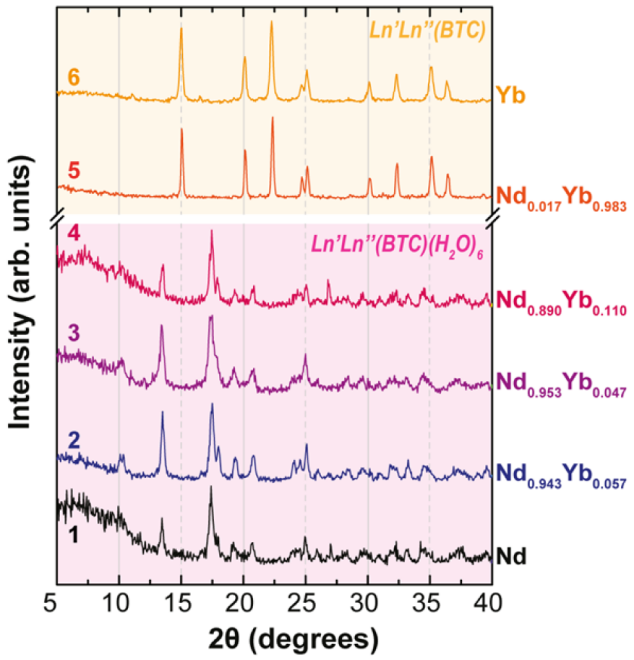

Figure 2. Powder X-ray diffraction patterns in the 5−40° 2θ range.

10000 for MOFs). Thus, as anticipated, our materials are nonporous and, accordingly, cannot be classified as MOFs.[53,54]

FT-IR spectra of **1**−**6** CPs show the typical bands assigned to the symmetric and antisymmetric stretching vibrations of carboxylic groups of trimesic acid[55] (near 1700 cm^{-1} and in the 1650−1550 and 1450−1350 cm^{-1} ranges, Figure S4). Since carboxylates can coordinate in different modes (monodentate, bidentate, bridging, etc.), the frequency separation between the carboxylate antisymmetric and symmetric stretching vibrations ($\Delta\nu_{a\text{-}s}$) can be related to the different coordination modes.[56] In fact, in **1**−**6**, $\Delta\nu_{a\text{-}s}$ (falling in the 170−180 cm^{-1} range) can be assigned, in agreement with the aforementioned crystal structures, to the bridging coordination mode. All **1**−**6** CPs show Ln−O stretching vibrational bands in the 600−400 cm^{-1} region.[57]

Thermogravimetric Analysis. TGA thermograms of **1** and **6** were measured to study the thermal stability and confirm the water content of the two representative structures. **1** shows four weight losses: a first one (below 70 °C) of about 1.5%, related to residual moisture; a second one of about 20% at 106 °C, and a third one of 4% at 298 °C, consistent with the elimination of the six water molecules. At higher temperatures, 500−700 °C, probably the three carboxylate groups are lost, as previously reported for metal-BTC MOFs,[58,59] and a 40% weight loss is attributed to the decomposition to Nd_2O_3 (Figure S5a). The thermogram of **6** confirms the absence of water in the structure and its thermal stability up to 400 °C. A 6% sharp loss at about 420 °C is due to a small amount of trimesic acid impurity (see Figure 2, PXRD peak at about 11°). A further increase in the temperature led to a >40% weight loss, with the formation of Yb_2O_3 above 500 °C (Figure S5b). Variable temperature X-ray diffraction analyses, described in detail in Text S2, enabled structural variations and quantitative measurement of anisotropic thermal expansion effects, demonstrating, *inter alia*, the stability range of these materials when heated in air.

Photophysical Properties. To further probe the presence of both metals in the same CPs, diffuse reflectance (DR) spectra were performed in the 200−2000 nm range. DR spectra of **1**−**6** show absorption bands at ∼1970, 1660, and 290 nm, due to the BTC linker. In **1**−**4** compounds (reported in Figure S7a), the absorption bands of Nd^{III} ions are observed at 872 nm ($^4I_{9/2} \rightarrow {}^4F_{3/2}$), 798 nm ($^4I_{9/2} \rightarrow {}^4F_{5/2}$), 740 nm ($^4I_{9/2} \rightarrow {}^4F_{7/2}$), 680 nm ($^4I_{9/2} \rightarrow {}^4F_{9/2}$), 578 nm ($^4I_{9/2} \rightarrow {}^2G_{7/2}$), 524 nm ($^4I_{9/2} \rightarrow {}^4G_{7/2} + {}^4G_{9/2}$), 513 nm ($^4I_{9/2} \rightarrow {}^4G_{9/2}$), and 355 nm ($^4I_{9/2} \rightarrow {}^4D_{5/2} + {}^4D_{3/2}$). In **2**−**4**, a further band at 980 nm is observed, confirming the presence of Yb^{III} ($^2F_{7/2} \rightarrow {}^2F_{5/2}$) in the CPs.[60−62] Compound **5** shows the absorption bands of both Nd^{III} and Yb^{III} ions when compared to **6**, which exhibits only the Yb^{III} absorption band, as shown in Figure S7.

Figure 3A shows the emission spectra of **1**, **4**, and **5**. Compounds **1** and **4** show the typical Nd^{III} emission bands related to the $^4F_{3/2} \rightarrow {}^4I_{11/2}$ transition.[46,62] In the case of **4**, Yb^{III} is present and the Yb^{III} $^2F_{5/2} \rightarrow {}^2F_{7/2}$ emission appears as a faint band at 980 nm.[46] However, this band is not present in compound **5** due to (i) the low concentration of Nd^{III} ions once the excitation is at 580 nm and (ii) the presence of a center of inversion at the Ln^{III} site (O_h point group symmetry) in the $Nd_xYb_{(1-x)}(BTC)$ structure (Figure S13b). The presence of a center of inversion does not affect the magnetic dipole transitions but affects the electric dipole interaction.[63] Thus, from selection rules on J quantum number ($|J - J'| = 0$ or 1), it is expected that the Nd^{III} $^4F_{3/2} \rightarrow {}^4I_J$ (J = 13/2, 11/2, 9/2) emissions present very weak intensities with vibronic and quadrupole[64] as main interactions. This spectroscopic feature could also be observed from the poor emission intensity and emission quantum yield (Table S5) of **5** regarding the second-order emission peak at 1160 nm (Figure S12) while Figure S10 shows that the second-order peaks are weaker for non-centrosymmetric CPs. The emission quantum yields for direct excitation in Nd^{III} (808 nm) and Yb^{III} (980 nm) are 0.022 ± 0.002% and 0.0030 ± 0.0003% (Table S5).

Among the compounds containing mostly Nd^{III} ions (**2**−**4**), **4** is the most promising system for ratiometric temperature measurement because of its higher emission intensity and emission quantum yield (Table S5), when compared to those of the other samples. Moreover, it presents a larger variation of relative intensities with temperature. The temperature-dependent photoluminescence intensity was studied to establish its potential as a new luminescent thermometer. The thermometric properties of the $Nd_xYb_{(1-x)}(BTC)$ compounds were not investigated due to their low emission intensities, as discussed before.

Compound **4** shows two bands at 980 and 1058 nm (Figure 3A), attributed to the Yb^{III} $^2F_{5/2} \rightarrow {}^2F_{7/2}$ and Nd^{III} $^4F_{3/2} \rightarrow {}^4I_{11/2}$ transitions, respectively. The relative intensity of Yb^{III} increases when decreasing the temperature and slight changes in the relative intensities between Yb^{III} and Nd^{III} emission bands at 1000 and 1057 nm, respectively, are observed at different temperatures (Figure 4B).

Additionally, at 300 K, the Yb^{III} and Nd^{III} emission lifetimes in **4** are $\tau_{Yb}(4) = 7.0 \pm 0.3$ μs and $\tau_{Nd}(4) = 51 \pm 1$ ns, respectively, as reported in Figure 3B,C. The short lifetime of Nd^{III} $^4F_{3/2}$ can be attributed to a strong electron−phonon interaction[65−67] and, once it depends on the material, it was also detected in **1** ($\tau_{Nd}(1) = 50 \pm 1$ ns, Figure S11).

This reflects a misapprehension of the usage of eqs 1 and 2 for estimations of experimental energy transfer and efficiencies. Furthermore, with the help of theoretical $Nd^{III} \rightarrow Yb^{III}$ energy transfer calculations, we will show in the next section that eqs 1

https://doi.org/10.1021/acs.chemmater.4c00362
Chem. Mater. 2024, 36, 3452−3463

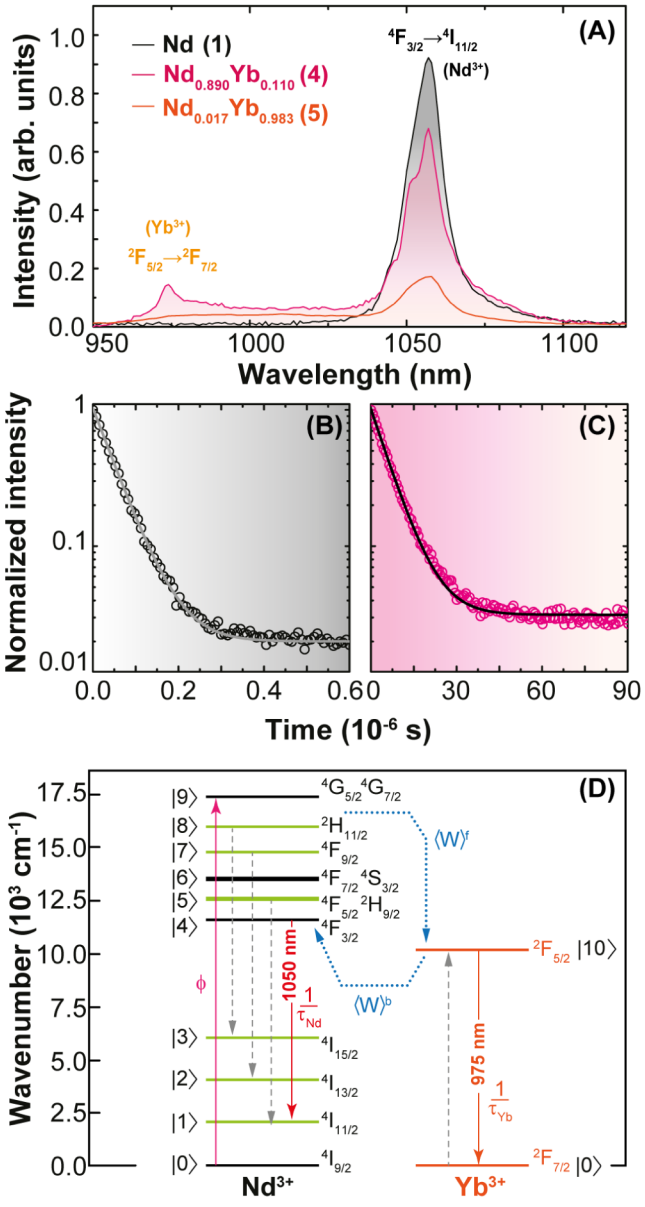

Figure 3. (A) Room temperature emission spectra of **1**, **4**, and **5** upon 580 nm excitation. Temporal dynamics decay traces of **4** upon 801 nm laser excitation monitoring the Nd^{III} and Yb^{III} emitting levels at (B) 1058 nm ($^4F_{3/2}$) and (C) 975 nm ($^2F_{5/2}$). (D) Jablonski-type energy level diagram depicting the Nd–Yb energy transfer process. ϕ is the pumping rate $^4I_{9/2} \rightarrow [^4G_{5/2}, ^2G_{7/2}]$ when Nd^{III} is excited at 580 nm. τ_{Nd} and τ_{Yb} are the decay lifetimes of the Nd^{III} and Yb^{III} emitting levels, respectively. $\langle W \rangle^f$ and $\langle W \rangle^b$ are the average Nd^{III}-to-Yb^{III} forward and backward energy transfer rates, respectively. The dashed straight lines on the Nd^{III} side (involving the green levels) are the main energy transfer pathways that have more contributions to $\langle W \rangle$. These rates consider the amount of each ion and their distribution in the compound.

and 2 using the Nd^{III} $^4F_{3/2}$ decay lifetimes are no longer valid because the energy transfer pathways involving this level represent less than 1% of the whole $Nd^{III} \rightarrow Yb^{III}$ energy transfer process. Consequently, this aspect enables the extraction of Yb^{III} $^2F_{5/2} \rightarrow {}^2F_{7/2}$ integrated intensity (I_{Yb}) by simple subtraction of the whole integrated area from 950 to 1100 nm by Nd^{III} $^4F_{3/2} \rightarrow {}^4I_{11/2}$ in **1** (Figure 4A), as it will be presented in the Luminescence thermometry subsection.

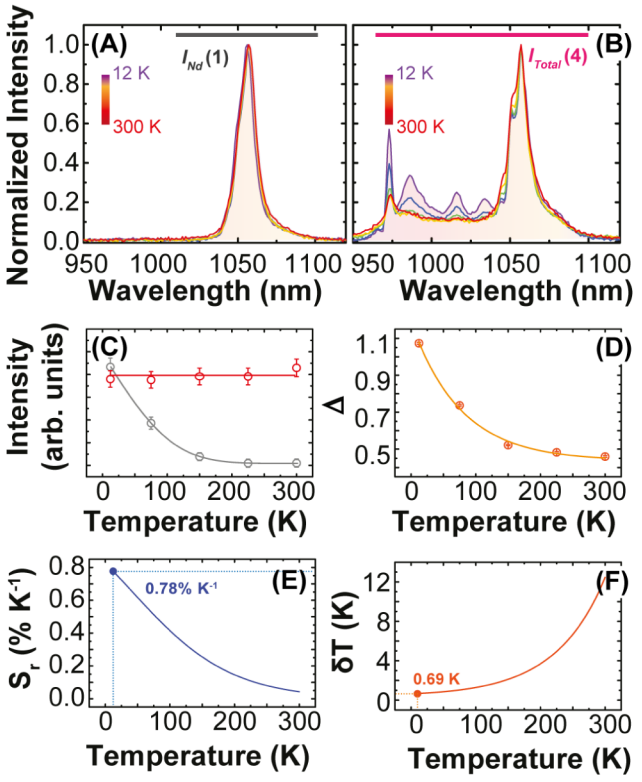

Figure 4. Emission spectra of (A) **1** and (B) **4** recorded in the 12–300 K range under 580 nm excitation. (C) Temperature dependence of I_{Yb} (in gray) and I_{Nd} (in red) integrate intensities. (D) Thermometric parameter $\Delta = I_{Yb}/I_{Nd}$. (E) Relative sensitivity S_r and (F) temperature uncertainty δT for **4**.

Nd^{III}-to-Yb^{II} Energy Transfer. The energy transfer (ET) rates between a pair of lanthanide ions were calculated considering the Kushida–Malta model,[68,69] which considers dipole–dipole (W_{d-d}), dipole–quadrupole (W_{d-q}), quadrupole–quadrupole (W_{q-q}), exchange (W_{ex}), and magnetic dipole–magnetic dipole (W_{md-md}) mechanisms, as defined by eqs S9–S13, respectively.[39,69] The ET pathways were selected according to energy mismatch conditions (donor–acceptor energy difference, δ, in Table S7) and selection rules on the J quantum numbers:

- Electric dipole interactions follows the traditional Judd–Ofelt[70,71] selection rule: $|J - J'| \leq \lambda \leq J + J'$ (with λ = 2, 4, and 6);
- Electric quadrupole interactions: $|J - J'| \leq 2$;
- Magnetic dipole interaction: $|J - J'| = 0$ or 1 (except the case of $J = J' = 0$).

There are no defined selection rules for the isotropic contribution of the exchange mechanism (W_{ex}).[69]

For an illustration of how the above selection rules work, consider pathway 17 in Tables S8–S11, which involves the donor transition $^4F_{3/2} \rightarrow {}^4I_{11/2}$ (Nd^{III}) transferring energy to the acceptor transition $^2F_{7/2} \rightarrow {}^2F_{5/2}$ (Yb^{III}) (Figure 3D). We can expect contributions from the W_{d-d} mechanism because both transitions obey the electric dipole selection rule. The squared reduced matrix elements $\langle {}^4I_{11/2} \| U^{(\lambda)} \| {}^4F_{3/2} \rangle^2$ are nonzero for λ = 4 and 6 (see Table S12) since $4 \leq \lambda \leq 7$ (for this Nd^{III} transition). Similarly, the Yb^{III} transition has contributions from all $\langle {}^2F_{5/2} \| U^{(\lambda)} \| {}^2F_{7/2} \rangle^2$ because $1 \leq \lambda \leq 6$.

https://doi.org/10.1021/acs.chemmater.4c00362
Chem. Mater. 2024, 36, 3452–3463

However, the dipole−quadrupole mechanism for the same pathway only has the contribution of the first term of eq S10 (donor by electric dipole and acceptor by electric quadrupole) because $\langle {}^4I_{11/2}\|U^{(2)}\|{}^4F_{3/2}\rangle^2 = 0$, annulling the second term (donor by quadrupole and acceptor by dipole). Similarly, the ET rate for the quadrupole−quadrupole mechanism (W_{q-q}, eq S11) for this pathway is zero since the selection rule on J for the donor transition is not fulfilled ($|11/2 - 3/2| > 2$ does not satisfy the condition $|J - J'| \leq 2$).

The sum of all mechanisms for a given pathway p (e.g., Nd^{III} $[{}^4F_{3/2} \rightarrow {}^4I_{9/2}] \Rightarrow Yb^{III}$ $[{}^2F_{7/2} \rightarrow {}^2F_{5/2}]$) is expressed as $\omega(p)$, while the sum of all pathways is defined as the total pairwise energy transfer rate $W = \sum \omega$. Tables S8−S11 show the pairwise energy transfer rates for the Nd−Yb distances of 5.85, 7.03, 7.26, and 8.66 Å, respectively. In these tables, each pathway "p" (i.e., a calculated ET rate consisting of one donor transition and one acceptor transition) is labeled as $\omega_i^l(p)$, where the superscript letter "l" represents the energy transfer direction (f and b stand for forward and backward) and the subscript "i" represents the Nd^{III}−Yb^{III} distances order from the crystallographic structure (i= 1, 2, 3, and 4 for respective of $R(i)$= 5.85, 7.03, 7.26, and 8.66 Å). W_i^l is the sum of all 64 ET pathways. Thus, as an example, W_1^f is the forward $Nd^{III} \rightarrow Yb^{III}$ energy transfer when Nd^{III}−Yb^{III} distance is 5.85 Å.

Concerning the ET pathways with contributions from the Nd^{III} ${}^4F_{3/2}$ level (i.e., ${}^4F_{3/2} \rightarrow {}^4I_J$, pathways p= 1, 17, 33, and 49 in Tables S8−S11), the sum of them together for each Nd−Yb distance are 410, 95, 75, and 19 s^{-1} which represents 0.7%, 1.0%, 1.0%, and 1.4% of the total ET rate, respectively. This result implies that transitions from Nd^{III} ${}^4F_{3/2}$ level are not important for the case of the Nd^{III}−Yb^{III} ET process and, as a result, the usage of eqs 1 and 2, considering the lifetime of this level, is not enough to estimate the experimental rate and efficiency. On the other hand, the most relevant ET pathways are from $[{}^2H_{11/2} \rightarrow {}^4I_{15/2}]$, $[{}^4F_{9/2} \rightarrow {}^4I_{13/2}]$, and $[{}^2H_{9/2}/{}^4F_{5/2} \rightarrow {}^4I_{11/2}]$ transitions (see pathways 55, 38, and 18/19 in Tables S8−S11), representing respectively around 85%, 7%, and 7% of the total Nd−Yb ET rate. It is worth mentioning that eqs 1, 2 are still valid for other lanthanide pairs in which the main donor level is the emitting one, such as the case of Tb−Eu, where the Tb^{III} ${}^5D_4$ level has an important contribution to the energy transfer process.[39,41] The dominant mechanism governing the energy transfer process is the W_{q-q}, with pairwise forward (Nd^{III}-to-Yb^{III}) ET rates for pathway 55 (Nd^{III} $[{}^2H_{11/2} \rightarrow {}^4I_{15/2}] \Rightarrow Yb^{III}$ $[{}^2F_{7/2} \rightarrow {}^2F_{5/2}]$ in Tables S8−S11) of 1.8×10^5, 2.8×10^4, 2.0×10^4, and 3.5×10^3 s^{-1} corresponding to Nd^{III}−Yb^{III} distances of 5.85, 7.03, 7.26, and 8.66 Å, respectively. The W_{q-q} mechanism is also responsible for the backward ET (Yb^{III}-to-Nd^{III}) process.

Once the pairwise Nd^{III}−Yb^{III} ET rates are calculated (Tables S8−S11), we can simulate a Monte Carlo type distribution of the coordinates of Nd^{III} and Yb^{III} ions in the host matrix by a homemade program written in C language (it can be provided upon request). From the crystallographic data of **1** ($Nd(BTC)(H_2O)_6$ sample), the unit cell ($1 \times 1 \times 1$) was expanded to a large one ($20 \times 20 \times 20$, Figure S14) with a volume of ≈10378 nm^3 containing 32000 Nd^{III} host sites, which can be replaced randomly by Yb^{III} until reaching the dopant amount desired (in %). Consequently, the occurrence of Nd−Yb pair as a function of distance n and concentration $1 - x$ of Yb^{III} throughout the matrix can be obtained and, consequently, the average forward $\langle W \rangle^f$ and backward $\langle W \rangle^b$ energy transfer rates:[41,72]

$$\langle W \rangle^{\mathrm{f}} = \sum_i \langle W \rangle_i^{\mathrm{f}} = (1 - x) \cdot x \left(\sum_i O_i (1 - x) W_i^{\mathrm{f}} \right) \tag{3}$$

$$\langle W \rangle^{\mathrm{b}} = \sum_i \langle W \rangle_i^{\mathrm{b}} = (1 - x) \cdot x \left(\sum_i O_i (x) W_i^{\mathrm{b}} \right) \tag{4}$$

where, as mentioned before, W_i^{f} stands for the forward and W_{i}^b for the backward energy transfer for the i^{th} Nd−Yb distance (Tables S8−S11). The acceptor Yb^{III} and the donor/host Nd^{III} stoichiometric fractions are represented by $1 - x$ and x, respectively. The occurrence coefficients O_i are related to the formation of a Nd−Yb pair at distance $R(i)$, regarding the acceptor (for forward energy transfer $\langle W \rangle^f$) or donor (for backward energy transfer $\langle W \rangle^b$) amount obtained from hundreds of Monte Carlo simulations for each Yb^{III} amount:[41,72]

$$O_i(1 - x) = \frac{\mathcal{N}(i)}{s \cdot (1 - x)}$$

$$O_i(x) = \frac{\mathcal{N}(i)}{s \cdot x} \tag{5}$$

where $\mathcal{N}(i)$ is the counting of Nd−Yb pairs at distance $R(i)$ and s is the number of host sites in the undoped matrix (equals 32000 host sites in the $20 \times 20 \times 20$ expanded cell, Figure S14a). Once the backward energy transfer is related to the energy coming from the Yb^{III} to the Nd^{III} ions, the 'acceptor' in this case is Nd^{III} and it justifies the use of the coefficients $O_i(x)$ instead of $O_i(1 - x)$ to calculate the $\langle W \rangle^b$. All values of O_i obtained from simulations as well as $\langle W \rangle^f$ and $\langle W \rangle^b$ are presented in Table S13.

Figure S15a shows the total calculated $\langle W \rangle^b$ with the changing of the Yb^{III} and Nd^{III} stoichiometric fractions while Figure S15b shows only the contribution of the backward Yb^{III} $[{}^2F_{5/2} \rightarrow {}^2F_{7/2}] \Rightarrow Nd^{III}$ $[{}^4I_{15/2} \rightarrow {}^2H_{11/2}]$ pathway, which is responsible for the quenching of the Yb^{III} emission when temperature increases, as observed in Figure 4B. The backward $\langle W \rangle^b$ is very sensitive to the temperature changes due to the contribution of about 89% of pathway 55 (Nd^{III} $[{}^2H_{11/2} \rightarrow {}^4I_{15/2}] \Rightarrow Yb^{III}$ $[{}^2F_{7/2} \rightarrow {}^2F_{5/2}]$, Tables S8−S11), which has a close resonant energy mismatch δ (Table S7). Our simulations varied the Yb^{III} amount as given by the synthesized samples ($1 - x$ = 0.047; 0.057; 0.110; representing, respectively, the (**3**); (**2**); (**4**); samples) and we also extrapolated until $1 - x$ = 0.200 to see the trend of the ET rates. For values of Yb^{III} doped above this limit, the $Nd_xYb_{(1-x)}(BTC)$ structure starts to appear (Figure S2), and once this phase has a Ln^{III} placed at a centrosymmetric site (Figure S13b), the emission of the Ln^{III} is quenched.[64] This is the reason we limited the simulations up to $1 - x$ = 0.200.

Estimation of the emitting level populations (e.g., Nd^{III} ${}^4F_{3/2}$ and Yb^{III} ${}^2F_{5/2}$) requires an effort to build and solve a set of coupled ordinary differential equations (ODEs) where the main rates are included, such as Ln−Ln energy transfer, radiative rates, and multiphonon relaxations. The transient of

https://doi.org/10.1021/acs.chemmater.4c00362
Chem. Mater. 2024, 36, 3452−3463

one level P_k is represented by solving an 11-level system of rate equations (eqs S19−S29). There are many numerical methods for solving a set of coupled ordinary differential equations;[73] however, we have been using the Radau method[74] because it provided fast and accurate results that were in excellent agreement with other Ln-based luminescence processes.[75−81]

Experimental and Theoretical Luminescence Thermometry. Considering the thermal dependence of this energy transfer from Nd^{III} to Yb^{III}, such systems can be exploited as ratiometric thermometers. First, emission of **1** was studied at different temperatures, as reported in Figure S10, showing a relatively weak signal at 1058 nm, assigned to the Nd^{III} $^4F_{9/2} \rightarrow {}^4I_{11/2}$ transition, upon 580 nm excitation. The intensity of the signal is weak considering the excitation of the second order around 1160 nm as a reference and, in this case, no significant changes were observed when decreasing the temperature.

Figure 4A, B displays the temperature dependence from 12 K up to 300 K of **1** and **5** emission spectra upon 580 nm lamp excitation. For both samples, it can be observed that the Nd^{III} $^2F_{3/2} \rightarrow {}^4I_{11/2}$ intensity has little temperature dependence, remaining almost constant (I_{Nd} in Figure 4C). Thus, the intensity of the Yb^{III} $^2F_{5/2} \rightarrow {}^2F_{7/2}$ (I_{Yb}) transition in sample **4** can be obtained by the subtraction of the integrated intensity I_{Nd} (highlighted area in Figure 4A) by the integrated intensity I_{Total} (highlighted area in Figure 4B). This can be assumed because the Nd^{III} $^2F_{3/2} \rightarrow {}^4I_{11/2}$ transition is not predominant in the $Nd^{III} \rightarrow Yb^{III}$ ET process, as indicated by theoretical calculations.

The distinct temperature dependence of I_{Yb} and I_{Nd} indicates that the intensity ratio I_{Yb}/I_{Nd} is temperature-sensitive and can be used as the thermometric parameter (Δ) for **4**.[6] Figure 4D shows the temperature evolution of Δ. As the temperature increases Δ decreases in the 12 to 220 K range, remaining constant at this temperature until 300 K, meaning that **4** is temperature-sensitive in the cryogenic range up to 220 K, and mostly insensitive beyond 220 K. The thermal performance of **4** was evaluated through the relative thermal sensitivity (S_r), and the temperature uncertainty (δT), which are the figures of merit to fully characterize the performance of an optical temperature sensor.[5,6,24]

Figure 4E displays S_r decreasing with temperature from a maximum value of 0.8%·K^{-1} at 12 K, reaching less than 0.1%·K^{-1} from 250 K and beyond, suggesting the temperature operative range of **4** as optical sensors ranges from 12 K up to 220 K, with a minimum δT of 0.7 at 12 K (Figure 4F). Despite the scarcity of reports on Nd^{III}−Yb^{III} systems for luminescence thermometry in the cryogenic temperature range, the S_r values presented in this study are comparable to those previously reported (Table S4). Likewise, the main advantage of our approach is the possibility to rationalize this thermometric performance in terms of the underneath energy transfer processes, as discussed in the following section.

The theoretical thermometric parameters of Nd^{III}/Yb^{III} mixed CPs were modeled through (i) energy transfer rates between Ln ions,[39,41,69,72] (ii) Judd−Ofelt intensity parameters,[82,83] (iii) Miyakawa−Dexter approach for multiphonon decay rates,[84] and (iv) rate equations modeling.[78,85−88] These building blocks allow us to estimate the relative emission intensity of Yb^{III} (I_{Yb}) and Nd^{III} (I_{Nd}), resulting in the theoretical thermometric parameter $\Delta = I_{Yb}/I_{Nd}$.

Figure S17a is presented for illustrative purposes and shows a comparison between the experimental and theoretical Δ values for sample **4**, assuming $\tau_{Nd} \approx 50$ ns and $\tau_{Yb} \approx 7.0$ μs (as measured at room temperature, Figure S11) for all temperatures in our simulations. The discrepancies observed at lower temperatures, indicated by red arrows (Figure S17a), suggest that the lifetimes, particularly τ_{Nd}, should be longer. This observation aligns with the temperature dependence of the electron−phonon coupling. To address these discrepancies, Figure S17b demonstrates the mitigation achieved in the simulations by considering longer lifetimes for both τ parameters in the low-temperature range below 150 K.

Furthermore, utilizing these theoretical curves, we can deduce that for temperatures below 150 K, the behavior of Δ is primarily governed by the Nd^{III}−Yb^{III} energy transfer, specifically the backward rates involving the Nd^{III} $^2H_{11/2}$ level. On the other hand, at high temperatures, the dominant factor influencing the thermometric parameter is the shortening of τ. This unusual shortening of τ_{Nd} to the order of 50 ns may potentially be attributed to thermally activated phonons coupling with Nd^{III} $^4F_{3/2}$, resulting in a fast depopulation of this level.

Figure 5 shows the simulated surfaces of Δ and S_r as a function of Yb^{3+} content and temperature. Comparing the highlighted curve in Figure 5A,B (representing the simulation

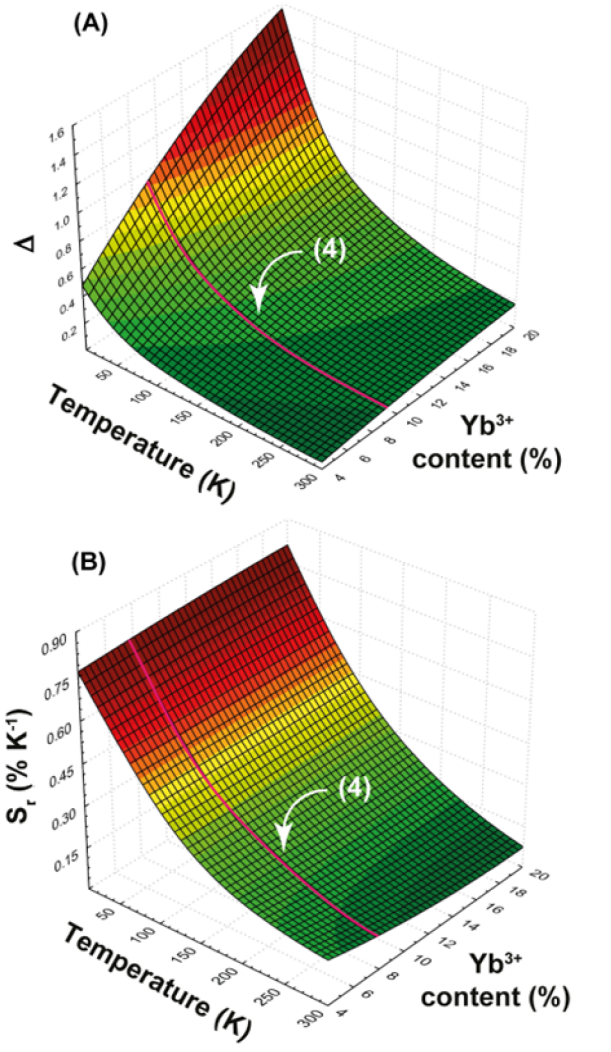

Figure 5. Theoretical (A) thermometric parameter Δ and (B) relative thermal sensitivity S_r as a function of temperature and Yb^{III} amount. The magenta lines indicate the simulated curves for **4**.

https://doi.org/10.1021/acs.chemmater.4c00362
Chem. Mater. 2024, 36, 3452−3463

for sample **4**) with Figure 4D,E, there is a significant agreement between the theoretical and experimental data. This finding supports the earlier discussed point in this article, namely, the limited involvement of the Nd^{III} $^4F_{3/2}$ level in the energy transfer process. Consequently, eqs 1 and 2 , which typically describe energy transfer rates and efficiencies between Ln ions, do not apply to Nd−Yb interactions unless the excitation occurs directly in the Nd^{III} $^4F_{3/2}$ level, not involving the Nd^{III} levels above.

CONCLUSIONS

Two different classes of CPs, formulated, respectively, as $Nd_xYb_{(1-x)}(BTC)(H_2O)_6$ (x = 1 (**1**); x = 0.943 (**2**); x = 0.953 (**3**); x = 0.890 (**4**)) and $Nd_xYb_{(1-x)}(BTC)$ (x = 0.017 (**5**), x = 0 (**6**)), were fully characterized by using a multitechnique approach to study their structure, morphology, composition, thermal stability, and optical properties. Particularly, **4** and **5** were selected to perform variable temperature photoluminescence studies in the 10−300 K range, which revealed a decrease of intensity ratio Nd^{III}/Yb^{III}-related emission upon increasing the temperature. This trend is more evident in **4**, which is therefore the most promising system within the entire series to be employed as a thermometer. The operative range of the **4** luminescent thermometer ranges from 12 up to 220 K, with a minimum δT of 0.69 at 12 K. However, rather than emphasizing the thermometric performance of **4**, the objective of the work is to fully understand the underlying energy transfer mechanisms and their crucial implications for optimizing energy transfer-driven ratiometric luminescent thermometers.

Then, theoretical calculations suggested that the Nd−Yb nonradiative energy transfer comes from a different and unexpected pathway for both forward (Nd^{III} [$^2H_{11/2}$ → $^4I_{15/2}$] → Yb^{III} [$^2F_{7/2}$ → $^2F_{5/2}$]) and backward (Yb^{III} [$^2F_{5/2}$ → $^2F_{7/2}$] → Nd^{III} [$^4I_{15/2}$ → $^2H_{11/2}$]) energy transfer. The immediate outcome of these calculations is that eqs 1 and 2 are not always valid to estimate the energy transfer rates and efficiency for Nd−Yb-based materials. Furthermore, the temperature dependency of $Nd_xYb_{(1-x)}(BTC)(H_2O)_6$ CPs is strongly influenced by the backward pathway and this corroborates with the observed quenching of the Yb^{III} emission when temperature increases. This is the first time that a complete ET analysis on the Nd−Yb pair was done where simulations of Ln'-to-Ln″ ET-driven thermometers were in good agreement with the experimental data. Remarkably the present joint experimental/theoretical work has the potential to pave the way to a rationalization of NIR luminescent thermometers based on Nd−Yb energy transfer.

EXPERIMENTAL SECTION

Materials. Lanthanide nitrates and the 1,3,5-benzenetricarboxylic acid were purchased from Alfa Aesar and Sigma-Aldrich, and then used without further purification.

Synthesis. All $Nd_xYb_{(1-x)}BTC(H_2O)_6$ (x = 1 (**1**); x = 0.943 (**2**); x = 0.953 (**3**); x = 0.890 (**4**)) and $Nd_xYb_{(1-x)}BTC$ (x = 0.017 (**5**), x = 0 (**6**)) compounds were prepared according to the previously reported method[48] as follows: 0.5 mmol of Ln^{III} precursor ($Nd(NO_3)_3{\cdot}6H_2O$ for **1** and $Yb(NO_3)_3{\cdot}6H_2O$ for **6**) was mixed with 0.5 mmol of H_3BTC (1,3,5-benzenetricarboxylic acid) and ground in an agate mortar for 5 min. Then the mixture was transferred into a 25 mL boron-silicate vial and heated at 130 °C for 24 h. After cooling to room temperature, the powder was collected and washed with distilled water and ethanol two times each and then dried at 60 °C for 3 h. For the synthesis of compounds **2**−**5**, the procedure was the same but the two Ln^{III} nitrates were mixed in different Nd/Yb stoichiometric ratios: from 95/5 to 80/20 (**2**−**4**) and 5/95 (**5**). The syntheses here proposed typically provide the final products in 100−300 mg amounts and are highly reproducible. Therefore, using batches from parallel preparations can easily lead to the accumulation of gram-sized samples. The conventional pathway to obtain these materials involves the use of hydrothermal methods. Although ancillary to this work, these recipes are here presented: compounds **1** and **6** were synthesized via a hydrothermal approach. A mixture of $Ln(NO_3)_3{\cdot}6(H_2O)$ (Ln^{III} = Nd Yb, (0.05 mmol), H_3BTC (0.15 mmol), NaOH (1,5 mmol), and water (25 mL) was heated at 120 °C for 24 h in a 50 mL Teflon-lined stainless-steel autoclave reactor. After cooling, a white powder, suitable for further characterizations, was obtained.

ICP-MS. Inductively coupled plasma spectroscopy (ICP) was performed on an Agilent Technologies ICP-MS 7900 spectrometer. The samples were prepared by using microwave digestion in an acid solution (5 mg of sample in 500 μL of concentrated HNO_3) followed by dilution with water (5 mL final volume).

Infrared Spectroscopy. FT-IR spectra were collected using a Bruker Equinox 55 spectrometer, with the samples prepared as KBr pellets (Figure S4).

Brunauer−Emmett−Teller (BET) Analyses. The textural properties were studied by nitrogen adsorption−desorption isotherms at −196 °C, measured on a Micromeritics ASAP 2020 system. The samples were preheated under vacuum at 50 °C (heating rate, 1 °C·min^{-1}) for 12 h. BET SSA values found: 37 $m^2{\cdot}g^{-1}$ for Nd(BTC)-$(H_2O)_6$ and 20 $m^2{\cdot}g^{-1}$ for Yb(BTC) (Text S3).

EDX Microanalysis. SEM images and EDX Microanalysis were performed both on a Hitachi S-4800 and ESEM:FEI Quanta 200 field emission scanning electron microscopes (Tables S2−S3 and Figure S6).

Thermogravimetric Analysis. Thermogravimetric analysis was performed in alumina crucibles with the instrument STA-6000 under nitrogen flux (40 mL/min) in the 25−800 °C temperature range at 10 °C/min.

Powder X-Ray Diffraction. PXRD patterns for fingerprinting purposes were collected by using a $\theta-\theta$ Bragg−Brentano geometry Seifert X 3000 diffractometer equipped with a Cu Kα source (λ = 1.5418 Å), a graphite monochromator on the diffracted beam, and a scintillation counter. Step size 0.05°, acquisition time 2 s/step. Structural PXRD studies required a more careful sample preparation, data collection strategy, and several computational steps (indexing, structure solution, and Rietveld refinement), collectively presented in the SI file. CSD Codes: 2212923−2212924.

Dynamic Light Scattering (DLS). The suspensions of Nd/Yb CPs in water/DMSO were prepared by suspending 2 mg of microcrystalline powder in 2 mL of solvent and ultrasonicating it for 15 min. Then they were diluted (200 μL of suspension and 800 μL of solvent) to allow DLS performed with the Malvern ZETASIZER NANO instrument.

Photophysical Measurements. Continuous-wave diffuse reflectance of crystals of coordination compounds was performed with a dual-beam spectrophotometer equipped with an integrating sphere accessory (Agilent Cary 5000 UV−vis−NIR). Emission and excitation spectra were recorded on a modular double grating excitation spectrofluorimeter with a TRIAX 320 emission monochromator (Fluorolog-3, Horiba Scientific) coupled to an NIR H9170 Hamamatsu photomultiplier, using the front face acquisition mode. The excitation source was a 450 W xenon arc lamp. The excitation spectra were corrected for the spectral distribution of the lamp intensity by using a photodiode reference detector. Time-resolved measurements were carried out with pulsed Xe−Hg lamp excitation in front face acquisition mode. The low-temperature measurements (12 K) were performed using a helium-closed cycle cryostat with a vacuum system measuring ca. 5×10^{-6} mbar and a Lakeshore 330 autotuning temperature controller with a resistance heater.

https://doi.org/10.1021/acs.chemmater.4c00362
Chem. Mater. 2024, 36, 3452−3463

THEORETICAL SECTION

Nd−Yb Energy Transfer. The pairwise energy transfer rates for Nd−Yb are calculated from eqs S9−S13 according to the procedures described in refs.[39,69] (see Supporting Information for more details). The distribution of Nd^{III} and Yb^{III} and the average energy transfer rates (from the pairwise Nd−Yb rates) were calculated using the method described in ref.[41].

Multiphonon Decay Rates. The nonradiative decay rates between adjacent levels of Nd^{III} ion were calculated using the Miyakawa−Dexter model as described in Supporting Information and ref 84.

Rate Equations. A general differential rate equation has the general form:[78,85−88]

$$\frac{d}{dt}P_k(t) = \sum_{j\neq k} W_{j\to k}P_j(t) - \sum_{j\neq k} W_{k\to j}P_k(t) \tag{6}$$

where the summations run the levels of the system. P_k and P_j are the populations of the levels $|k\rangle$ and $|j\rangle$, $W_{j\to k}$ and $W_{k\to j}$ are rates between these states (Nd^{III}−Yb^{III} energy transfer or decay processes). The first summation represents all rates that enter in $|k\rangle$, while the second represents those that depart from $|k\rangle$. The complete set of the rate equation model is given by the coupled equations (eqs S19−S29).

Intensity Parameters and Radiative Rates. The Judd−Ofelt intensity parameters were calculated using the Simple Overlap Model (SOM)[83] for the odd component of the ligand field and the Bond Overlap Model (BOM)[82] for the polarizability-dependent term. The radiative rates are calculated using eqs S31−S33 (see Supporting Information for further details).

Thermometric Parameter and Relative Thermal Sensitivity. The experimental Δ was defined as $\Delta = I_{Yb}/I_{Nd}$, where I_{Yb} and I_{Nd} are the integrated intensity of the $^2F_{5/2} \rightarrow {}^2F_{7/2}$ and $^4F_{3/2} \rightarrow {}^4I_{11/2}$ emissions, respectively. Thus, the theoretical Δ is given by

$$\Delta = \frac{I_{Yb}}{I_{Nd}} = \frac{A_{rad}(Yb)}{A_{rad}(Nd)}\cdot\frac{P_{10}}{P_4} \tag{7}$$

where A_{rad} is the radiative component of the $^2F_{5/2} \rightarrow {}^2F_{7/2}$ and $^4F_{3/2} \rightarrow {}^4I_{11/2}$ transitions. P_{10} and P_4 represent the calculated populations of the Yb^{III} $^2F_{5/2}$ and Nd^{III} $^4F_{3/2}$ emitting levels in the steady-state regime, respectively. The thermal sensitivity is given by

$$S_r = \frac{1}{\Delta}\left|\frac{\partial\Delta}{\partial T}\right| \tag{8}$$

as defined for the experimental one.

ASSOCIATED CONTENT

Supporting Information

The Supporting Information is available free of charge at https://pubs.acs.org/doi/10.1021/acs.chemmater.4c00362

Powder X-ray diffraction; FT-IR spectra; thermogravimetric analysis; EDX microanalysis, ICP-MS data, and SEM images; photophysical characterization; materials stability by DLS and PXRD measurements; performance of Nd^{III}/Yb^{III}-based luminescent thermometers; photoluminescent properties; theoretical modeling methodology; supplementary text 1: an estimate of specific surface areas; supplementary text 2: thermal stability in air; supplementary text 3: textural properties (PDF)

crystallographic data of **1** $(Nd(BTC)(H_2O)_6)$ (CIF)

crystallographic data of $Nd_xYb_{(1-x)}(BTC)(H_2O)_6$ (CIF)

AUTHOR INFORMATION

Corresponding Authors

Albano N. Carneiro Neto − *Phantom-g, Department of Physics, CICECO-Aveiro Institute of Materials, University of Aveiro, Aveiro 3810-193, Portugal;* orcid.org/0000-0003-2432-0992; Email: albanoneto@ua.pt

Luís D. Carlos − *Phantom-g, Department of Physics, CICECO-Aveiro Institute of Materials, University of Aveiro, Aveiro 3810-193, Portugal;* orcid.org/0000-0003-4747-6535; Email: lcarlos@ua.pt

Maria Laura Mercuri − *Dipartimento di Scienze Chimiche e Geologiche, Università degli Studi di Cagliari, Monserrato I-09042, Italy; INSTM, Firenze 50121, Italy;* orcid.org/0000-0002-4816-427X; Email: mercuri@unica.it

Authors

Mariangela Oggianu − *Dipartimento di Scienze Chimiche e Geologiche, Università degli Studi di Cagliari, Monserrato I-09042, Italy; INSTM, Firenze 50121, Italy*

Valentina Mameli − *Dipartimento di Scienze Chimiche e Geologiche, Università degli Studi di Cagliari, Monserrato I-09042, Italy; INSTM, Firenze 50121, Italy*

Miguel A. Hernández-Rodríguez − *Phantom-g, Department of Physics, CICECO-Aveiro Institute of Materials, University of Aveiro, Aveiro 3810-193, Portugal*

Noemi Monni − *Dipartimento di Scienze Chimiche e Geologiche, Università degli Studi di Cagliari, Monserrato I-09042, Italy; INSTM, Firenze 50121, Italy*

Manuel Souto − *Department of Chemistry, CICECO-Aveiro Institute of Materials, University of Aveiro, Aveiro 3810-193, Portugal;* orcid.org/0000-0003-3491-6984

Carlos D.S. Brites − *Phantom-g, Department of Physics, CICECO-Aveiro Institute of Materials, University of Aveiro, Aveiro 3810-193, Portugal;* orcid.org/0000-0001-9636-2628

Carla Cannas − *Dipartimento di Scienze Chimiche e Geologiche, Università degli Studi di Cagliari, Monserrato I-09042, Italy; INSTM, Firenze 50121, Italy;* orcid.org/0000-0003-2908-7739

Fabio Manna − *Dipartimento di Scienze Chimiche e Geologiche, Università degli Studi di Cagliari, Monserrato I-09042, Italy*

Francesco Quochi − *INSTM, Firenze 50121, Italy; Dipartimento di Fisica, Università degli Studi di Cagliari, Monserrato I-09042, Italy*

Enzo Cadoni − *Dipartimento di Scienze Chimiche e Geologiche, Università degli Studi di Cagliari, Monserrato I-09042, Italy*

Norberto Masciocchi − *Dipartimento di Scienza e Alta Tecnologia & To.Sca.Lab., Università degli Studi dell, Como 22100, Italy;* orcid.org/0000-0001-9921-2350

Complete contact information is available at: https://pubs.acs.org/10.1021/acs.chemmater.4c00362

Author Contributions

[▽]M.O., V.M., and M.A.H.-R. have contributed equally to this work. The manuscript was written through the contributions of

https://doi.org/10.1021/acs.chemmater.4c00362
Chem. Mater. 2024, 36, 3452−3463

all authors. All authors have approved the final version of the manuscript.

Funding

Fondazione di Sardegna—Convenzione triennale tra la Fondazione di Sardegna e gli Atenei Sardi, Regione Sardegna—L.R. 7/2007 annualità 2020, through Project 'Smart supramolecular Materials for Anion sensing and Water Remediation (SMAWRT),' CUP: F75F21001260007, is acknowledged for financial support. FCT/MCTES—The Shape of Water (PTDC/NAN-PRO/3881/2020), LogicALL (PTDC/CTM-CTM/0340/2021) and RedoxMOFs (PTDC/QUI-ELT/2593/2021) financed by Portuguese funds.

Notes

The authors declare no competing financial interest.

■ ACKNOWLEDGMENTS

This work was developed within the scope of the projects CICECO-Aveiro Institute of Materials, UIDB/50011/2020 (DOI 10.54499/UIDB/50011/2020), UIDP/50011/2020 (DOI 10.54499/UIDP/50011/2020) & LA/P/0006/2020 (DOI 10.54499/LA/P/0006/2020), The Shape of Water (PTDC/NAN-PRO/3881/2020), LogicALL (PTDC/CTM-CTM/0340/2021) and RedoxMOFs (PTDC/QUI-ELT/2593/2021) financed by national funds through the FCT/MCTES (PIDDAC). This work has also received funding from the European Research Council (grant agreement no. 101039748). CeSAR (Centro Servizi d'Ateneo per la Ricerca) *core facility* of the University of Cagliari is acknowledged for the use of the Scanning Electron Microscopy Laboratory. Prof. Miguel Clemente-Leon, University of Valencia, is also acknowledged for ICP-MS data and helpful discussion. PON AIM (PON Ricerca e Innovazione 2014−2020 − Azione I.2 − DD n. 407 del 27 febbraio 2018 "Attraction and International Mobility", Cult-GeoChim project AIM1890410-3), and CESA project are gratefully acknowledged for financing the fellowships of V. Mameli. CeSAR (Centro Servizi d'Ateneo per la Ricerca) of the University of Cagliari, Italy, is also acknowledged for ESEM-EDX measurements performed with of FEI Company Quanta 200 ESEM equipped with a Thermo Scientific EDX probe.

■ ABBREVIATIONS

CP	coordination polymer
MOF	metal−organic framework
H_3BTC	1,3,5-benzentricarboxylic acid
NIR	near-infrared
ET	energy transfer
PXRD	powder X-ray diffractometry
ICP-MS	induced coupled plasm mass spectrometry
SEM-EDX	scanning electron microscopy—energy dispersive X-ray
TGA	thermal gravimetric analysis
FT-IR	Fourier transformed—infrared spectroscopy
DR	diffuse Reflectance spectra

■ REFERENCES

(1) Michalski, L.; Eckersdorf, K.; Kucharski, J.; McGhee, J. *Temperature Measurement*, 2nd ed.; John Wiley & Sons: West Sussex, 2002.

(2) Moldover, M. R.; Tew, W. L.; Yoon, H. W. Advances in Thermometry. *Nat. Phys.* **2016**, *12* (1), 7−11.

(3) Dedyulin, S.; Ahmed, Z.; Machin, G. Emerging Technologies in the Field of Thermometry. *Meas. Sci. Technol.* **2022**, *33* (9), 092001.

(4) Bednarkiewicz, A.; Marciniak, L.; Carlos, L. D.; Jaque, D. Standardizing Luminescence Nanothermometry for Biomedical Applications. *Nanoscale* **2020**, *12* (27), 14405−14421.

(5) Brites, C. D. S.; Lima, P. P.; Silva, N. J. O.; Millán, A.; Amaral, V. S.; Palacio, F.; Carlos, L. D. Thermometry at the Nanoscale. *Nanoscale* **2012**, *4* (16), 4799.

(6) Brites, C. D. S.; Balabhadra, S.; Carlos, L. D. Lanthanide-Based Thermometers: At the Cutting-Edge of Luminescence Thermometry. *Adv. Opt. Mater.* **2019**, *7* (5), 1801239.

(7) Nexha, A.; Carvajal, J. J.; Pujol, M. C.; Díaz, F.; Aguiló, M. Lanthanide Doped Luminescence Nanothermometers in the Biological Windows: Strategies and Applications. *Nanoscale* **2021**, *13* (17), 7913−7987.

(8) Dramićanin, M. D. Trends in Luminescence Thermometry. *J. Appl. Phys.* **2020**, *128* (4), 040902.

(9) Elliott, G. D.; Wang, S.; Fuller, B. J. Cryoprotectants: A Review of the Actions and Applications of Cryoprotective Solutes That Modulate Cell Recovery from Ultra-Low Temperatures. *Cryobiology* **2017**, *76*, 74−91.

(10) Afonso, J.; Martins, D.; Catarino, I.; Patrício, R.; Rocaboy, A.; Tirolien, T.; Bonfait, G. Liquid−Gas Cryogenic Energy Storage Units Operating at Constant Temperature. *Appl. Therm. Eng.* **2016**, *95*, 178−185.

(11) Potts, C. A.; Bittencourt, V. A. S. V.; Kusminskiy, S. V.; Davis, J. P. Magnon-Phonon Quantum Correlation Thermometry. *Phys. Rev. Appl.* **2020**, *13* (6), 064001.

(12) Kale, A.; Khanna, N. A Review on Cryogenic Machining of Super Alloys Used in Aerospace Industry. *Procedia Manuf.* **2017**, *7*, 191−197.

(13) Giordano, V.; Fluhr, C.; Dubois, B. Magnetic Sensitivity of the Microwave Cryogenic Sapphire Oscillator. *J. Appl. Phys.* **2020**, *127* (18), 184101.

(14) Rosso, L.; Tabandeh, S.; Beltramino, G.; Fernicola, V. Validation of Phosphor Thermometry for Industrial Surface Temperature Measurements. *Meas. Sci. Technol.* **2020**, *31* (3), 034002.

(15) Quintanilla, M.; Henriksen-Lacey, M.; Renero-Lecuna, C.; Liz-Marzán, L. M. Challenges for Optical Nanothermometry in Biological Environments. *Chem. Soc. Rev.* **2022**, *51* (11), 4223−4242.

(16) Bao, G.; Wong, K.-L.; Jin, D.; Tanner, P. A. A Stoichiometric Terbium-Europium Dyad Molecular Thermometer: Energy Transfer Properties. *Light: sci. Appl.* **2018**, *7* (1), 96.

(17) Hasegawa, Y.; Kitagawa, Y. Thermo-Sensitive Luminescence of Lanthanide Complexes, Clusters, Coordination Polymers and Metal−Organic Frameworks with Organic Photosensitizers. *J. Mater. Chem. C* **2019**, *7* (25), 7494−7511.

(18) Gu, Y.; Piñol, R.; Moreno-Loshuertos, R.; Brites, C. D. S.; Zeler, J.; Martínez, A.; Maurin-Pasturel, G.; Fernández-Silva, P.; Marco-Brualla, J.; Téllez, P.; et al.et al. Local Temperature Increments and Induced Cell Death in Intracellular Magnetic Hyperthermia. *ACS Nano* **2023**, *17* (7), 6822−6832.

(19) Savchuk, O. A.; Carvajal, J. J.; Massons, J.; Cascales, C.; Aguiló, M.; Díaz, F. Novel Low-Cost Compact and Fast Signal Processing Sensor for Ratiometric Luminescent Nanothermometry. *Sens. Actuators, A* **2016**, *250*, 87−95.

(20) Cui, Y.; Xu, H.; Yue, Y.; Guo, Z.; Yu, J.; Chen, Z.; Gao, J.; Yang, Y.; Qian, G.; Chen, B. A Luminescent Mixed-Lanthanide Metal−Organic Framework Thermometer. *J. Am. Chem. Soc.* **2012**, *134* (9), 3979−3982.

(21) Cadiau, A.; Brites, C. D. S.; Costa, P. M. F. J.; Ferreira, R. A. S.; Rocha, J.; Carlos, L. D. Ratiometric Nanothermometer Based on an Emissive Ln^{3+}-Organic Framework. *ACS Nano* **2013**, *7* (8), 7213−7218.

(22) Brites, C. D. S.; Lima, P. P.; Silva, N. J. O.; Millán, A.; Amaral, V. S.; Palacio, F.; Carlos, L. D. Ratiometric Highly Sensitive Luminescent Nanothermometers Working in the Room Temperature Range. Applications to Heat Propagation in Nanofluids. *Nanoscale* **2013**, *5* (16), 7572.

(23) Ferdinandus; Suzuki, M.; Vu, C. Q.; Harada, Y.; Sarker, S. R.; Ishiwata, S.; Kitaguchi, T.; Arai, S. Modulation of Local Cellular

Activities Using a Photothermal Dye-Based Subcellular-Sized Heat Spot. *ACS Nano* **2022**, *16* (6), 9004−9018.
(24) Brites, C. D. S.; Millán, A.; Carlos, L. D. Lanthanides in Luminescent Thermometry. In *Handbook on the Physics and Chemistry of Rare Earths*, Bünzli, J.-C. G.; Pecharsky, V. K., Eds.; Elsevier, 2016; Vol. *49*, pp. 339427.
(25) Jia, M.; Chen, X.; Sun, R.; Wu, D.; Li, X.; Shi, Z.; Chen, G.; Shan, C. Lanthanide-Based Ratiometric Luminescence Nanothermometry. *Nano Res.* **2023**, *16* (2), 2949−2967.
(26) Bünzli, J.-C. G.; Piguet, C. Taking Advantage of Luminescent Lanthanide Ions. *Chem. Soc. Rev.* **2005**, *34* (12), 1048.
(27) Taarit, I.; Alves, F.; Benchohra, A.; Guénée, L.; Golesorkhi, B.; Rosspeintner, A.; Fürstenberg, A.; Piguet, C. Seeking Brightness in Molecular Erbium-Based Light Upconversion. *J. Am. Chem. Soc.* **2023**.
(28) Rocha, J.; Brites, C. D. S.; Carlos, L. D. Lanthanide Organic Framework Luminescent Thermometers. *Chem. - Eur. J.* **2016**, *22* (42), 14782−14795.
(29) Cui, Y.; Zhu, F.; Chen, B.; Qian, G. Metal−Organic Frameworks for Luminescence Thermometry. *Chem. Commun.* **2015**, *51* (35), 7420−7431.
(30) Kanzariya, D. B.; Chaudhary, M. Y.; Pal, T. K. Engineering of Metal−Organic Frameworks (MOFs) for Thermometry. *Dalt. Trans.* **2023**, *52* (22), 7383−7404.
(31) Orlova, A. V.; Kozhevnikova, V. Y.; Goloveshkin, A. S.; Lepnev, L. S.; Utochnikova, V. V. NIR Luminescence Thermometers Based on Yb−Nd Coordination Compounds for the 83−393 K Temperature Range. *Dalt. Trans.* **2022**, *51* (14), 5419−5425.
(32) Xiang, G.; Yang, M.; Liu, Z.; Wang, Y.; Jiang, S.; Zhou, X.; Li, L.; Ma, L.; Wang, X.; Zhang, J. Near-Infrared-to-Near-Infrared Optical Thermometer BaY_2O_4: Yb^{3+}/Nd^{3+} Assembled with Photothermal Conversion Performance. *Inorg. Chem.* **2022**, *61* (13), 5425−5432.
(33) Gomez, G. E.; Marin, R.; Carneiro Neto, A. N.; Botas, A. M. P.; Ovens, J.; Kitos, A. A.; Bernini, M. C.; Carlos, L. D.; Soler-Illia, G. J. A. A.; Murugesu, M. Tunable Energy-Transfer Process in Heterometallic MOF Materials Based on 2,6-Naphthalenedicarboxylate: Solid-State Lighting and Near-Infrared Luminescence Thermometry. *Chem. Mater.* **2020**, *32* (17), 7458−7468.
(34) Suo, H.; Zhao, X.; Zhang, Z.; Guo, C. Ultra-Sensitive Optical Nano-Thermometer $LaPO_4$: Yb^{3+}/Nd^{3+} Based on Thermo-Enhanced NIR-to-NIR Emissions. *Chem. Eng. J.* **2020**, *389*, 124506.
(35) Gao, G.; Busko, D.; Kauffmann-Weiss, S.; Turshatov, A.; Howard, I. A.; Richards, B. S. Wide-Range Non-Contact Fluorescence Intensity Ratio Thermometer Based on Yb^{3+}/Nd^{3+} Co-Doped La_2O_3 Microcrystals Operating from 290 to 1230 K. *J. Mater. Chem. C* **2018**, *6* (15), 4163−4170.
(36) Xu, W.; Hu, Y.; Zheng, L.; Zhang, Z.; Cao, W.; Liu, H.; Wu, X. Enhanced NIR-NIR Luminescence from $CaWO_4$: Nd^{3+}/Yb^{3+} Phosphors by Li^+ Codoping for Thermometry and Optical Heating. *J. Lumin.* **2019**, *208*, 415−423.
(37) Chen, H.; Bai, G.; Yang, Q.; Hua, Y.; Xu, S.; Chen, L. Non-Contact Fluorescence Intensity Ratio Optical Thermometer Based on Yb^{3+}/Nd^{3+} Codoped $Bi_4Ti_3O_{12}$ Microcrystals. *J. Lumin.* **2020**, *221*, 117095.
(38) Xu, W.; Qi, H.; Zheng, L.; Zhang, Z.; Cao, W. Multifunctional Nanoparticles Based on the Nd^{3+}/Yb^{3+} Codoped $NaYF_4$. *Opt. Lett.* **2015**, *40* (23), 5678.
(39) Carneiro Neto, A. N.; Moura, R. T., Jr.; Shyichuk, A.; Paterlini, V.; Piccinelli, F.; Bettinelli, M.; Malta, O. L. Theoretical and Experimental Investigation of the $Tb^{3+} \rightarrow Eu^{3+}$ Energy Transfer Mechanisms in Cubic $A_3Tb_{0.90}Eu_{0.10}(PO_4)_3$ (A = Sr, Ba) Materials. *J. Phys. Chem. C* **2020**, *124* (18), 10105−10116.
(40) Jaque, D.; Ramirez, O.; Bausá, E.; Solé, G.; Cavalli, E.; Speghini, A.; Bettinelli, M. $Nd^{3+} \rightarrow Yb^{3+}$ Energy Transfer in the $YAl_3(BO_3)_4$ Nonlinear Laser Crystal. *Phys. Rev. B* **2003**, *68* (11), 1−9.
(41) Trannoy, V.; Carneiro Neto, A. N.; Brites, C. D. S.; Carlos, L. D.; Serier-Brault, H. Engineering of Mixed Eu^{3+}/Tb^{3+} Metal-Organic Frameworks Luminescent Thermometers with Tunable Sensitivity. *Adv. Opt. Mater.* **2021**, *9* (6), 2001938.
(42) Lupei, A.; Lupei, V.; Ikesue, A.; Gheorghe, C.; Hau, S. Nd → Yb Energy Transfer in (Nd, Yb): Y_2O_3 Transparent Ceramics. *Opt. Mater.* **2010**, *32* (10), 1333−1336.
(43) Artizzu, F.; Serpe, A.; Marchiò, L.; Saba, M.; Mura, A.; Mercuri, M. L.; Bongiovanni, G.; Deplano, P.; Quochi, F. Controlling Nd-to-Yb Energy Transfer through a Molecular Approach. *J. Mater. Chem. C* **2015**, *3* (43), 11524−11530.
(44) Lupei, A.; Lupei, V.; Ikesue, A.; Gheorghe, C. Spectroscopic and Energy Transfer Investigation of Nd/Yb in Y_2O_3 Transparent Ceramics. *J. Opt. Soc. Am. B* **2010**, *27* (5), 1002−1010.
(45) Balda, R.; Peña, J. I.; Arriandiaga, M. A.; Fernández, J. Efficient $Nd^{3+} \rightarrow Yb^{3+}$ Energy Transfer in $0.8CaSiO_3$-$0.2Ca_3(PO_4)_2$ Eutectic Glass. *Opt. Express* **2010**, *18* (13), 13842.
(46) Yue, D.; Zhang, J.; Zhao, D.; Lian, X.; Cui, Y.; Yang, Y.; Qian, G. Ratiometric near Infrared Luminescent Thermometer Based on Lanthanide Metal-Organic Frameworks. *J. Solid State Chem.* **2016**, *241*, 99−104.
(47) Guan, M.; Mei, L.; Huang, Z.; Yang, C.; Guo, Q.; Xia, Z. Synthesis and Near-Infrared Luminescence Properties of LaOCl: Nd^{3+}/Yb^{3+}. *Infrared Phys. Technol.* **2013**, *60*, 98−102.
(48) Liu, J.; Pei, L.; Xia, Z.; Xu, Y. Hierarchical Accordion-like Lanthanide-Based Metal−Organic Frameworks: Solvent-Free Syntheses and Ratiometric Luminescence Temperature-Sensing Properties. *Cryst. Growth Des.* **2019**, *19* (11), 6586−6591.
(49) Ying, P.; Yu, J.; Su, W. Liquid-Assisted Grinding Mechanochemistry in the Synthesis of Pharmaceuticals. *Adv. Synth. Catal.* **2021**, *363* (5), 1246−1271.
(50) Kosimov, A.; Yusibova, G.; Aruväli, J.; Paiste, P.; Käärik, M.; Leis, J.; Kikas, A.; Kisand, V.; Šmits, K.; Kongi, N. Liquid-Assisted Grinding/Compression: A Facile Mechanosynthetic Route for the Production of High-Performing Co−N−C Electrocatalyst Materials. *Green Chem.* **2022**, *24* (1), 305−314.
(51) Friščić, T.; Halasz, I.; Štrukil, V.; Eckert-Maksić, M.; Dinnebier, R. E. Clean and Efficient Synthesis Using Mechanochemistry: Coordination Polymers, Metal-Organic Frameworks and Metallodrugs. *Croat. Chem. Acta* **2012**, *85* (3), 367−378.
(52) Davies, K.; Bourne, S. A.; Oliver, C. L. Solvent- and Vapor-Mediated Solid-State Transformations in 1,3,5- Benzenetricarboxylate Metal − Organic Frameworks. *Cryst. Growth Des.* **2012**, *12*, 1999−2003.
(53) Biradha, K.; Ramanan, A.; Vittal, J. J. Coordination Polymers Versus Metal−Organic Frameworks. *Cryst. Growth Des.* **2009**, *9* (7), 2969−2970.
(54) Steed, J. W.; Atwood, J. L. *Supramolecular Chemistry*, 2nd ed.; Wiley: Chichester, UK, 2009.
(55) Mahalakshmi, G.; Balachandran, V. FT-IR and FT-Raman Spectra, Normal Coordinate Analysis and Ab Initio Computations of Trimesic Acid. *Spectrochim. Acta, Part A* **2014**, *124*, 535−547.
(56) Deacon, G. B.; Phillips, R. J. Relationships between the Carbon-Oxygen Stretching Frequencies of Carboxylato Complexes and the Type of Carboxylate Coordination. *Coord. Chem. Rev.* **1980**, *33* (3), 227−250.
(57) Kerim, F. M. A.; Aly, H. F.; El-Agramy, A. Infrared Absorption Spectra of Some Lanthanide Acetylacetonate Complexes. *Proc. Indian Acad. Sci.* **1977**, *85* (6), 559−566.
(58) Sahiner, N.; Demirci, S.; Yildiz, M. Preparation and Characterization of Bi-Metallic and Tri-Metallic Metal Organic Frameworks Based on Trimesic Acid and Co(II), Ni(II), and Cu(II) Ions. *J. Electron. Mater.* **2017**, *46* (2), 790−801.
(59) Sel, K.; Demirci, S.; Meydan, E.; Yildiz, S.; Ozturk, O. F.; Al-Lohedan, H.; Sahiner, N. Benign Preparation of Metal−Organic Frameworks of Trimesic Acid and Cu, Co or Ni for Potential Sensor Applications. *J. Electron. Mater.* **2015**, *44* (1), 136−143.
(60) Feng, W.; Zhang, Y.; Zhang, Z.; Su, P.; Lü, X.; Song, J.; Fan, D.; Wong, W. K.; Jones, R. A.; Su, C. Near-Infrared (NIR) Luminescent Metallopolymers Based on Ln 4(Salen)4 Nanoclusters (Ln = Nd or Yb). *J. Mater. Chem. C* **2014**, *2* (8), 1489.

https://doi.org/10.1021/acs.chemmater.4c00362
Chem. Mater. 2024, 36, 3452−3463

(61) Carnall, W. T. The Near-Infrared Transitions of the Trivalent Lanthanides in Solution. II. Tb^{+3}, Dy^{+3}, Ho^{+3}, Er^{+3}, Tm^{+3}, and Yb^{+3}. *J. Phys. Chem.* **1963**, *67* (6), 1206−1211.
(62) Rast, H. E.; Caspers, H. H.; Miller, S. A. Fluorescence and Energy Transfer between Nd^{3+} and Yb^{3+} in LaF_3. *J. Chem. Phys.* **1967**, *47* (10), 3874−3878.
(63) Ryba-Romanowski, W.; Golab, S.; Pisarski, W. A. Investigation of Infrared-to-Visible Conversion in Cubic $Cs_2NaErCl_6$ Crystals. *J. Phys.: Condens. Matter.* **1995**, *7* (37), 7397−7404.
(64) Carneiro Neto, A. N.; Moura, R. T.; Malta, O. L. On the Mechanisms of Non-Radiative Energy Transfer between Lanthanide Ions: Centrosymmetric Systems. *J. Lumin.* **2019**, *210*, 342−347.
(65) Padlyak, B. V.; Ryba-Romanowski, W.; Lisiecki, R.; Oseledchik, Y. S.; Prosvirnin, A. L.; Kudryavtcev, D. P.; Svitanko, N. V. Optical Spectroscopy of the Nd^{3+} Luminescence Centres in the $Sr_4B_{14}O_{25}$: Nd Crystal. *Acta Phys. Polym., A* **2010**, *117* (1), 104−110.
(66) Meijerink, A.; Blasse, G.; Sytsma, J.; Ellens, A. Electron—Phonon Coupling in Rare Earth Compounds. *ACTA Phys. Polym.,* A **1996**, *90* (1), 109−119.
(67) Karbowiak, M.; Sobczyk, M.; Drożdżyński, J. Comparison between Electron−Phonon Coupling Strengths of U^{3+} and Nd^{3+} Ions Doped in $LaCl_3$ and U^{3+} in $LaBr_3$ Single Crystals. *J. Solid State Chem.* **2003**, *173* (1), 59−68.
(68) Kushida, T. Energy Transfer and Cooperative Optical Transitions in Rare-Earth Doped Inorganic Materials. I. Transition Probability Calculation. *J. Phys. Soc. Jpn.* **1973**, *34* (5), 1318−1326.
(69) Malta, O. L. Mechanisms of Non-Radiative Energy Transfer Involving Lanthanide Ions Revisited. *J. Non-Cryst. Solids* **2008**, *354* (42−44), 4770−4776.
(70) Judd, B. R. Optical Absorption Intensities of Rare-Earth Ions. *Phys. Rev.* **1962**, *127* (3), 750−761.
(71) Ofelt, G. S. Intensities of Crystal Spectra of Rare-Earth Ions. *J. Chem. Phys.* **1962**, *37* (3), 511−520.
(72) Qin, X.; Carneiro Neto, A. N.; Longo, R. L.; Wu, Y.; Malta, O. L.; Liu, X. Surface Plasmon−Photon Coupling in Lanthanide-Doped Nanoparticles. *J. Phys. Chem. Lett.* **2021**, *12* (5), 1520−1541.
(73) Butcher, J. C. Numerical Methods for Ordinary Differential Equations in the 20th Century. *J. Comput. Appl. Math.* **2000**, *125* (1−2), 1−29.
(74) Hairer, E.; Wanner, G. Radau Methods. In*Encyclopedia of Applied and Computational Mathematics*, Engquist, B.; Springer: Berlin, Heidelberg, 2015; pp. 12131216.
(75) Fang, M.; Carneiro Neto, A. N.; Fu, L.; Ferreira, R. A. S.; de Zea Bermudez, V.; Carlos, L. D. A Hybrid Materials Approach for Fabricating Efficient WLEDs Based on Di-Ureasils Doped with Carbon Dots and a Europium Complex. *Adv. Mater. Technol.* **2022**, *7* (3), 2100727.
(76) Mamontova, E.; Botas, A. M. P.; Brites, C. D. S.; Ferreira, R. A. S.; Rouquette, J.; Guari, Y.; Larionova, J.; Long, J.; Carlos, L. D. Rationalizing the Thermal Response of Dual-Center Molecular Thermometers: The Example of an Eu/Tb Coordination Complex. *Adv. Opt. Mater.* **2022**, *10* (5), 2101870.
(77) Ramalho, J. F. C. B.; Dias, L. M. S.; Fu, L.; Botas, A. M. P.; Carlos, L. D.; Carneiro Neto, A. N.; André, P. S.; Ferreira, R. A. S. Customized Luminescent Multiplexed Quick-Response Codes as Reliable Temperature Mobile Optical Sensors for EHealth and Internet of Things. *Adv. Photonics Res.* **2022**, *3*, 2100206.
(78) Ramalho, J. F. C. B.; Carneiro Neto, A. N.; Carlos, L. D.; André, P. S.; Ferreira, R. A. S. Lanthanides for the New Generation of Optical Sensing and Internet of Things. In *Handbook on the Physics and Chemistry of Rare Earths*, Bünzli, J.-C. G.; Pecharsky, V. K., Eds.; Elsevier, 2022, pp. 31128.
(79) Kasprzycka, E.; Carneiro Neto, A. N.; Trush, V. A.; Malta, O. L.; Jerzykiewicz, L.; Amirkhanov, V. M.; Legendziewicz, J.; Gawryszewska, P. Spectroscopic Aspects for the Yb^{3+} Coordination Compound with a Large Energy Gap between the Ligand and Yb^{3+} Excited States. *Spectrochim. Acta, Part A* **2022**, *274*, 121072.
(80) Lyubov, D. M.; Carneiro Neto, A. N.; Fayoumi, A.; Lyssenko, K. A.; Korshunov, V. M.; Taydakov, I. V.; Salles, F.; Guari, Y.; Larionova, J.; Carlos, L. D.; et al. Employing Three-Blade Propeller Lanthanide Complexes as Molecular Luminescent Thermometers: Study of Temperature Sensing through a Concerted Experimental/Theory Approach. *J. Mater. Chem. C* **2022**, *10* (18), 7176−7188.
(81) Salerno, E. V.; Carneiro Neto, A. N.; Eliseeva, S. V.; Hernández-Rodríguez, M. A.; Lutter, J. C.; Lathion, T.; Kampf, J. W.; Petoud, S.; Carlos, L. D.; Pecoraro, V. L. Tunable Optical Molecular Thermometers Based on Metallacrowns. *J. Am. Chem. Soc.* **2022**, *144* (40), 18259−18271.
(82) Moura Jr, R. T.; Carneiro Neto, A. N.; Longo, R. L.; Malta, O. L. On the Calculation and Interpretation of Covalency in the Intensity Parameters of 4f-4f Transitions in Eu^{3+} Complexes Based on the Chemical Bond Overlap Polarizability. *J. Lumin.* **2016**, *170*, 420−430.
(83) Malta, O. L. A Simple Overlap Model in Lanthanide Crystal-Field Theory. *Chem. Phys. Lett.* **1982**, *87* (1), 27−29.
(84) Miyakawa, T.; Dexter, D. L. Phonon Sidebands Multiphonon Relaxation of Excited States, and Phonon-Assisted Energy Transfer between Ions in Solids. *Phys. Rev. B* **1970**, *1* (7), 2961−2969.
(85) Grant, W. J. C. Role of Rate Equations in the Theory of Luminescent Energy Transfer. *Phys. Rev. B* **1971**, *4* (2), 648−663.
(86) Ferreira, R. A. S.; Carneiro Neto, A. N.; Correia, S. F. H.; Carlos, L. D.Lanthanide Emission for Solar Spectral Converters: An Energy Transfer Viewpoint. In *Springer Series on Fluorescence*; Springer: Cham, 2021; pp. 133.
(87) Carneiro Neto, A. N.; Teotonio, E. E. S.; de Sá, G. F.; Brito, H. F.; Legendziewicz, J.; Carlos, L. D.; Felinto, M. C. F. C.; Gawryszewska, P.; Moura Jr, R. T.; Longo, R. L.; Faustino, W. M.; Malta, O. L. Modeling Intramolecular Energy Transfer in Lanthanide Chelates: A Critical Review and Recent Advances. In *Handbook on the Physics and Chemistry of Rare Earths*, Bünzli, J.-C. G.; Pecharsky, V. K., Eds.; Elsevier, 2019; Vol. *56*, pp. 55162.
(88) Blois, L.; Malta, O. L.; Brito, H. F. The Role of the Eu^{3+} $^7F_1$ Level in the Direct Sensitization of the $^5D_0$ Emitting Level through Intramolecular Energy Transfer. *J. Lumin.* **2022**, *247*, 118862.

https://doi.org/10.1021/acs.chemmater.4c00362
Chem. Mater. 2024, 36, 3452−3463